A rhombohedral ferroelectric phase in epitaxially strained Hf0.5Zr0.5O2 thin films

Wei, Yingfen; Nukala, Pavan; Salverda, Mart; Matzen, Sylvia; Zhao, Hong Jian; Momand, Jamo; Everhardt, Arnoud S.; Agnus, Guillaume; Blake, Graeme R.; Lecoeur, Philippe

Published in:
Nature Materials

DOI:
10.1038/s41563-018-0196-0

Publication date:
2018

nature materials

ARTICLES

https://doi.org/10.1038/s41563-018-0196-0

A rhombohedral ferroelectric phase in epitaxially strained $Hf_{0.5}Zr_{0.5}O_2$ thin films

Yingfen Wei[1], Pavan Nukala[1,2], Mart Salverda[1], Sylvia Matzen[3], Hong Jian Zhao[4], Jamo Momand[1], Arnoud S. Everhardt[1], Guillaume Agnus[3], Graeme R. Blake[1], Philippe Lecoeur[3], Bart J. Kooi[1], Jorge Íñiguez[4], Brahim Dkhil[2] and Beatriz Noheda[1*]

Hafnia-based thin films are a favoured candidate for the integration of robust ferroelectricity at the nanoscale into next-generation memory and logic devices. This is because their ferroelectric polarization becomes more robust as the size is reduced, exposing a type of ferroelectricity whose mechanism still remains to be understood. Thin films with increased crystal quality are therefore needed. We report the epitaxial growth of $Hf_{0.5}Zr_{0.5}O_2$ thin films on (001)-oriented $La_{0.7}Sr_{0.3}MnO_3/SrTiO_3$ substrates. The films, which are under epitaxial compressive strain and predominantly (111)-oriented, display large ferroelectric polarization values up to 34 μC cm^{-2} and do not need wake-up cycling. Structural characterization reveals a rhombohedral phase, different from the commonly reported polar orthorhombic phase. This finding, in conjunction with density functional theory calculations, allows us to propose a compelling model for the formation of the ferroelectric phase. In addition, these results point towards thin films of simple oxides as a vastly unexplored class of nanoscale ferroelectrics.

Ferroelectric materials exhibit switchable spontaneous polarization, and are of great technological interest for a myriad of applications, notably in microelectronics[1], spintronics[2] and micro/nano-electromechanical systems[3]. However, miniaturizing ferroelectrics is not an easy task, since depolarization fields become increasingly important at reduced sizes[4,5]. Searching for robust ferroelectric properties at the nanoscale has therefore been a recurrent challenge. Thus, the recent discovery of ferroelectricity in ultrathin layers of HfO_2-based materials[6] represents a real breakthrough in the field, and seems to expose a new type of ferroelectricity: one that appears only at the nanoscale and becomes stronger at smaller dimensions. In addition, silicon compatibility, the simplicity of their chemistry and low toxicity make them very attractive compared to the other commonly used ferroelectric layers.

In bulk, the stable form of HfO_2 (ZrO_2)-based compounds is a monoclinic phase ($P2_1/c$, m-phase) at room temperature[7,8]. Other common high-temperature and high-pressure phases, namely, tetragonal ($P4_2/nmc$, t-phase) and cubic ($Fm\bar{3}m$, c-phase) phases[7,8], can be stabilized at room temperature via doping[9] or nanostructuring[10,11]. In addition, rhombohedral phases (r-phase) have also been obtained by doping and applying mechanical stress[12–15]. The t- and r-phases are distortions from the fluorite structure (c-phase) and have a significantly lower volume than the m-phase. None of the above-mentioned phases is reported to be polar.

A polar orthorhombic phase ($Pca2_1$, o-phase) was first reported for Mg-doped ZrO_2 when cooled to cryogenic temperatures[16]. This polar phase is believed to be the structural origin for the recently reported ferroelectricity in HfO_2-based thin films[6]. Recent literature has gathered examples of these ferroelectric films with different dopants[17–19], on different substrates (Si (ref. [6]) and Y-ZrO_2 (ref. [20])), with different electrodes (that is, TiN (ref. [21]), Pt (ref. [22]), Ir (ref. [23]), TaN (ref. [24]) and Si (ref. [25])) and by different growth methods (for example, atomic layer deposition (ALD)[26], chemical solution deposition[27], pulsed laser deposition (PLD)[20] and chemical vapour deposition)[28]. Various possible mechanisms, such as stress[29,30], doping[24], confinement by the top electrode[21] or surface energy[31–33], were put forward as stabilizing factors for the ferroelectric phase.

Initially, the best ferroelectric properties were reported only in ultrathin films (usually around 10 nm thick)[26,34,35]. The polarization declined significantly with increasing thickness as a result of the nonpolar m-phase appearing[35]. More recently, ferroelectricity has been found in thicker films (50 to 390 nm)[27,36] where the average grain size is below 10 nm. Thus, all reported ferroelectric hafnia-based films have in common that they are formed by small crystallites, emphasizing the crucial role played by size effects in stabilizing the ferroelectric phase[33]. Indeed, it is known that in nanoparticles of radius r, the surface energy (σ) can produce large internal pressures ($P = 2\sigma/r$) of the order of gigapascals[37,38]. Thus, small crystals will prefer the room-temperature stability of lower-volume c- or t-phases to the m-phase[39–41]. For thicker films, usually above 10 nm (where the crystals have the possibility to grow further), the m-phase (bulk) is always present. The polar o-phase has been postulated as the transformation phase between the t- and m-phases[16,24,42].

Most works report on ALD-grown films, which are polycrystalline and contain multiple phases (m-, t- and o-phases). In addition, the similarity of these structures and the small size of crystallites make a complete structural characterization even more challenging. Therefore, well-oriented samples, preferably in a single phase, are desired to study the factors responsible for ferroelectricity. Single-crystal, epitaxial Y-doped HfO_2 films have been achieved by PLD on yttrium oxide-stabilized zirconium oxide substrates with the polar o-phase[20], reaching a polarization of 16 μC cm^{-2}. Here, we also utilize PLD to grow highly oriented ferroelectric $Hf_{0.5}Zr_{0.5}O_2$ (HZO) films on a perovskite $SrTiO_3$ (STO) substrate with $La_{0.7}Sr_{0.3}MnO_3$ (LSMO) as a back electrode to gain insights into the role of strain on the ferroelectricity in hafnia-based systems.

[1]Zernike Institute for Advanced Materials, University of Groningen, Groningen, the Netherlands. [2]Laboratoire Structures, Propriétés et Modélisation des Solides, CentraleSupélec, CNRS-UMR8580, Université Paris-Saclay, Gif-sur-Yvette, France. [3]Center for Nanoscience and Nanotechnology, CNRS-UMR 9001, Université Paris-Saclay, Palaiseau, France. [4]Materials Research and Technology Department, Luxembourg Institute of Science and Technology (LIST), Esch/Alzette, Luxembourg. *e-mail: b.noheda@rug.nl

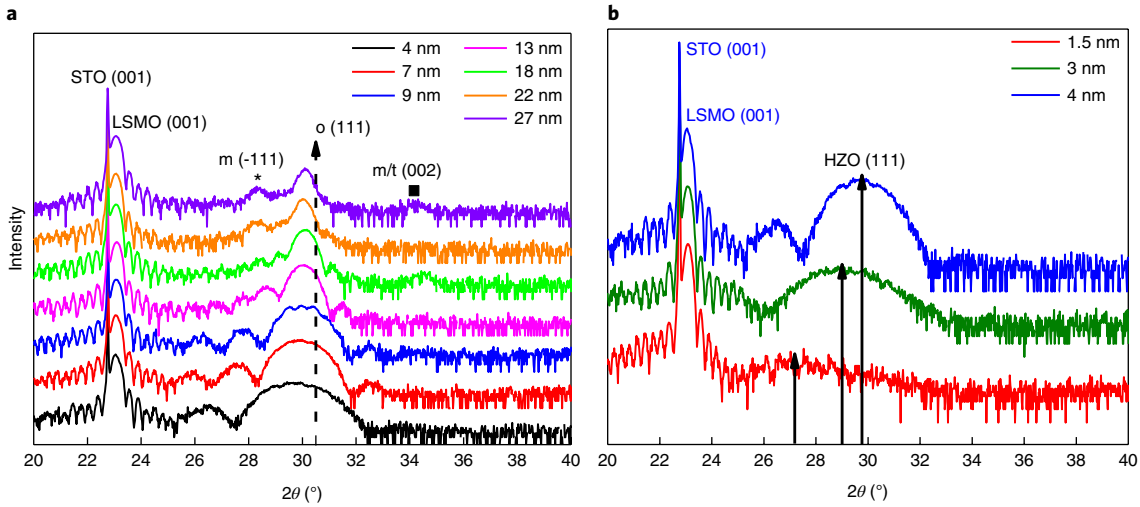

Fig. 1 | XRD structural characterization of HZO films on LSMO-buffered 001-oriented STO. a, Specular XRD pattern of HZO films with thicknesses ranging from 4 nm to 27 nm. **b**, Specular XRD patterns of HZO films with thicknesses ranging from 1.5 nm to 4 nm.

A rhombohedral phase of HZO

X-ray diffraction (XRD) θ–2θ patterns along the crystal truncation rod of HZO films with different thicknesses are shown in Fig. 1a. The highest peaks mark the (001) specular Bragg reflection of the STO substrate and the epitaxially grown LSMO bottom electrode with thickness of ~30 nm; the third largest feature is the main Bragg peak of the HZO films appearing at around 30°. The crystal truncation rods are visible in the form of thickness oscillations, which demonstrates the good crystalline quality and interfaces of the films. This 2θ value is slightly lower than that corresponding to the (111) reflection in the commonly reported polar o-phase in HZO, which appears at around 30.5° as shown by the black dashed line[35]. This indicates an expanded (111)-spacing (d_{111}) in the out-of-plane direction. In particular, extremely thin films below 4 nm (Fig. 1b) display highly elongated unit cells with the (111) reflection appearing at 2θ well below 30°. As the thickness decreases, the HZO (111) peaks shift rapidly to smaller angles (larger d-spacing), which indicates a huge compressive in-plane strain for the thinnest layers. For films thicker than 9 nm, new peaks appear (at 28.3° and 34°), which can be assigned to the m-phase, consistent with the stabilization of the m-phase with increasing crystal size (while increasing thickness)[35].

According to the XRD patterns, the films are (111)-oriented (Fig. 1). Pole figure (texture) measurements were performed around the {111} peaks in a 9-nm-thick film. In a (111)-oriented single-domain film, the other three reflections, (-111), (11-1) and (1-11), are expected at an angle (χ) of ~71° from the out-of-plane direction, with azimuthal angles (φ) differing by 120°. As seen in Fig. 2a, 12 reflections instead of 3 are found at $\chi \approx 71°$, revealing four crystallographic domains with different but well-defined in-plane orientations. The crystal domains are rotated 90° with respect to each other, following the four-fold symmetry of the (001)-oriented cubic substrate. In addition, four weak reflections at $\chi \approx 55°$ reveal a small amount of (001)-oriented component in the film. Synchrotron XRD was used to scan all 13 reflections in the pole figure, revealing that the 12 peaks with in-plane components of the scattering vector (at $\chi \approx 71°$) share the exact same $2\theta = 27.13°$ (Fig. 2b), giving rise to a d-spacing ($d_{11-1} = d_{1-11} = d_{-111} = 2.94$ Å) that is significantly smaller than that of the out-of-plane (111) reflection ($d_{111} = 2.98$ Å). Thus, these measurements reveal a multiplicity that is only consistent with a rhombohedral unit cell (Fig. 2c) and a polar (three-fold) axis out of the plane of the sample.

To gain further understanding of the structure, we performed transmission electron microscopy (TEM) and local spectroscopy studies. Plane-view selected-area electron diffraction (SAED), shown in Fig. 3a for a 9-nm-thick film, displays a superposition of diffraction patterns from at least two domains of HZO. The {220} spots from both domains occur at $\varphi = 45° + 60n$ (yellow circles in Fig. 3a) and at $\varphi = 15° + 60n$ (blue circles), with n being an integer from 0 to 5 (the $\varphi = 0°$ direction is defined as the $[100]_{STO}$ direction). HZO domains rotated 180° about the $[111]_{HZO}$ (// $[001]_{STO}$) direction give identical plane-view diffraction patterns ({220} spots with $d_{220} = 1.79$ Å in Fig. 3a). Thus, the SAED results are consistent with the existence of four domains rotated by 90° from each other around $[111]_{HZO}$ as is independently revealed by X-ray pole figure analysis in Fig. 2a. Furthermore, an epitaxial relation between the substrate and the film with $[1\text{-}10]_{HZO}//[1\text{-}10]_{STO}$, and $[11\text{-}2]_{HZO}//[110]_{STO}$, can be clearly identified.

Next, we performed cross-sectional high-angle annular dark-field scanning TEM (HAADF-STEM) analyses on 4-nm- and 9-nm-thick films, along zone axes defined by $\varphi = 0°$ ($[100]_{STO}$), $\varphi = 15°$ and $\varphi = 45°$ ($[110]_{STO}$). Figure 3b displays a HAADF-STEM image from a 9-nm-thick sample (zone axis, $\varphi = 45°$), clearly showing the coexistence of majority and minority HZO domains with the $[111]_{HZO}$ and $[001]_{HZO}$ out-of-plane, respectively, in agreement with the XRD data. From the fast Fourier transform (inset, Fig. 3b) across many images, we deduce that $d_{111} = 2.95$–3.01 Å and $d_{11-1} = 2.92$–2.96 Å. These values ($d_{111} \neq d_{11-1}$) provide a clear confirmation of the non-orthorhombic nature of this phase (see Supplementary Fig. 1 for analysis based on forbidden spots) and support the rhombohedral phase revealed by the synchrotron XRD measurements (Fig. 2b). Figure 3c displays a HAADF-STEM image from a 4-nm-thick sample (zone axis, $\varphi = 15°$), where we observe the coexistence of different (111)-oriented domains. Notably, (001)-oriented areas are only rarely found at these low thicknesses (see Supplementary Fig. 2).

We analysed the chemistry and structure of the interface between HZO and LSMO through energy-dispersive spectroscopy (EDS) performed in conjunction with HAADF-STEM. Comparison of the EDS chemical maps with the HAADF-STEM image (zone axis, $\varphi = 0°$) reveals the presence, at the interface with LSMO, of 2–3 monolayers of HZO that are in a different phase to the rest of the HZO film (Supplementary Fig. 3). This interfacial HZO phase is completely strained to the substrate ($a = 3.91$ Å), which corresponds

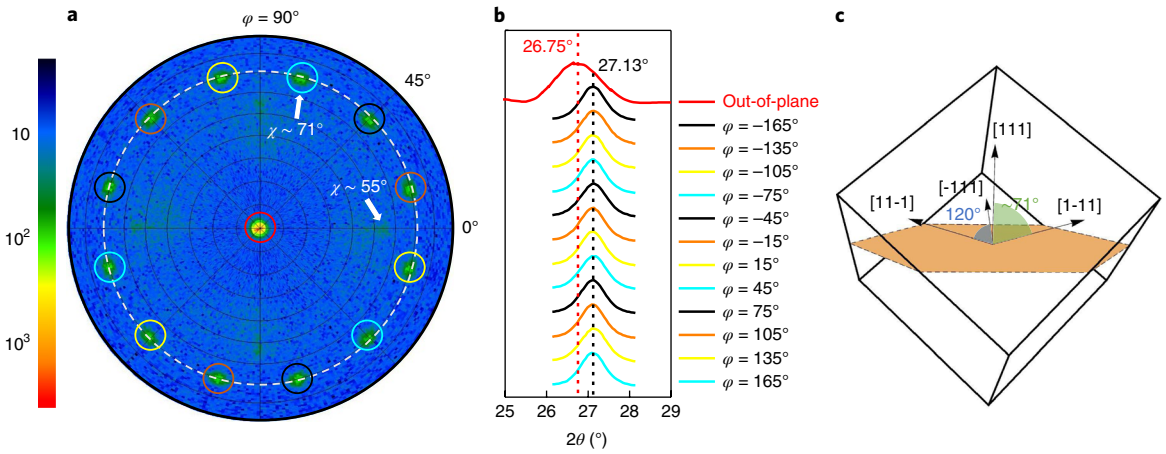

Fig. 2 | Domain configuration and symmetry. a, Pole figure around the (111) peak of a 9 nm HZO film at $2\theta = 29.98°$. The radial direction represents χ, which ranges between 0° and 90°, while the azimuthal direction represents φ, with a (0°–360°) range. Colour represents intensity in log scale (left). **b**, 2θ scans of the 13 peaks in the pole figure measured at the P08 High-Resolution Diffraction Beamline in PETRA III (DESY) with a wavelength of $\lambda = 1.378$ Å. **c**, Sketch of the proposed rhombohedral structure of the HZO film with polarization along the [111] direction.

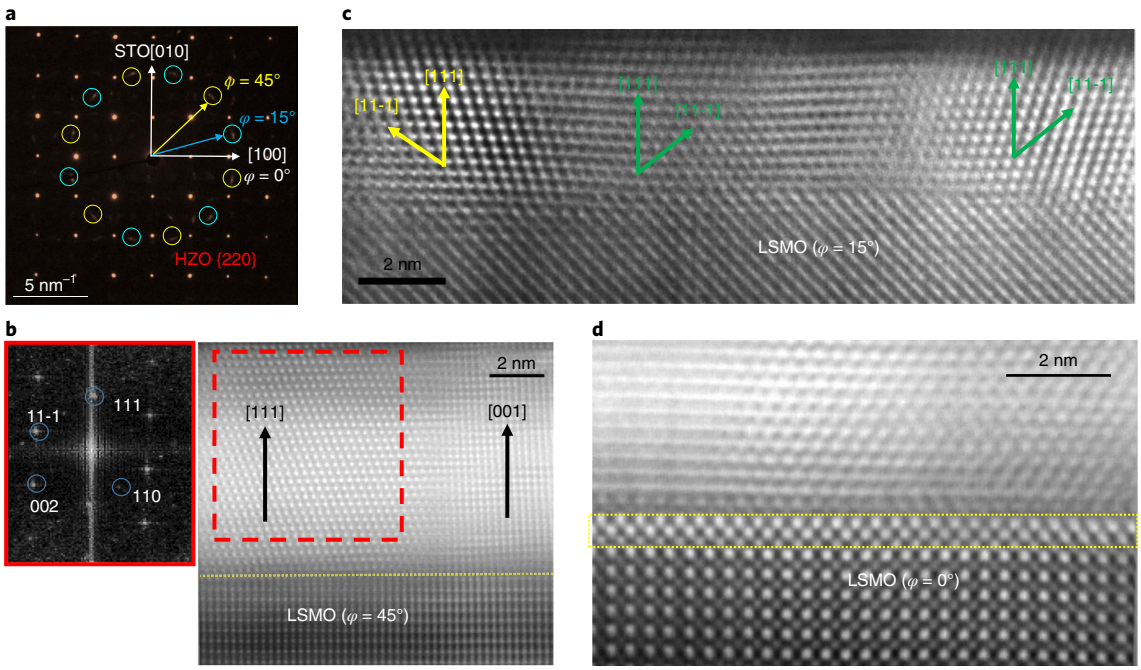

Fig. 3 | Electron microscopy characterization. a, Plane-view SAED pattern from a 9-nm-thick HZO sample. The out-of-plane direction is [111] (zone axis). The {220} spots ($d_{220} = 1.79$ Å), corresponding to at least two different domains (yellow and blue circles, respectively) rotated by 90° with respect to each other, can be clearly identified. **b**, Cross-sectional HAADF-STEM image (corrected for sample drift) of the 9-nm-thick HZO film, observed along the [110] zone of the substrate ($\varphi = 45°$). Inset (left): Fourier transform of the [111] domain. **c**, Representative cross-sectional HAADF-STEM image (drift-corrected) of a 4-nm-thick film, observed along the zone axis defined by $\varphi = 15°$. **d**, HAADF-STEM image observed along STO [100], revealing a clear interfacial t-phase of HZO (see EDX in Supplementary Fig. 3).

to a huge (~8%) in-plane tensile-strained t-phase ($a = 3.60$ Å in the unstrained t-phase), as shown in Fig. 3d (see also Supplementary Fig. 3c for HAADF simulations). This in-plane tensile strain results in a much lower out-of-plane parameter measured as $c/2 = 2.31$–2.44 Å (across several images), compared to the unstrained t-phase ($c = 5.12$ Å). An interfacial t-phase has previously been observed in ALD-synthesized doped-HfO_2 samples with TiN electrodes[43], and also on epitaxially strained Y-doped ZrO_2 films grown on STO[44]. After the above-mentioned two atomic layers at the interface, the r-phase grows under compressive strain. With increasing thickness, the m-phase in the [001]-orientation appears (Supplementary Fig. 4), also in agreement with the XRD data.

Ferroelectricity of rhombohedral HZO

To test the ferroelectric behaviour of the films, we obtained polarization versus voltage (P–V) loops through positive up negative down (PUND) measurements (Supplementary Fig. 5). Bistable switching and hysteresis loops can be observed in Fig. 4 for 5-nm- and 9-nm-thick films. After subtracting the non-ferroelectric switching contribution, the blue lines show only the ferroelectric switching

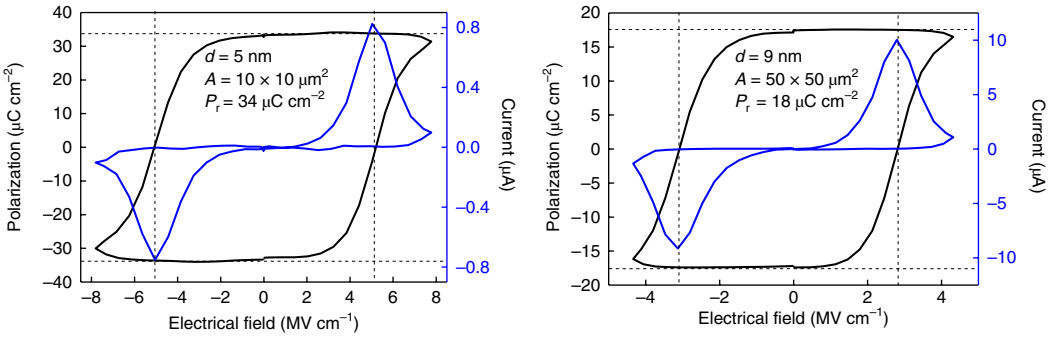

Fig. 4 | Ferroelectric characterization. PUND measurements (see Supplementary Information) of 5-nm-thick (left) and 9-nm-thick (right) films under an electric field of frequency 1 kHz are shown. The blue lines are the current (I) versus voltage (V) curves after extracting the non-ferroelectric switching response; the black lines are the integrated signal giving rise to the corresponding P–V hysteresis loops.

current with coercive field, E_c, around 5 MV cm^{-1} and 3 MV cm^{-1}, respectively, consistent with the expected dependence of E_c on thickness (d) as $E_c \propto d^{-2/3}$. The coercive fields are larger than the 1 MV cm^{-1} reported in ALD-grown films[21]. This could be due to the dead layers at the interface with the LSMO electrodes, as discussed previously, and/or the clamping effect from the strained epitaxial film. However, the coercive field itself does not increase on cycling (see Supplementary Fig. 6).

The largest remanent polarization (P_r) values among all doped-hafnia compositions have been obtained in La-doped and Gd-doped HfO_2 films[17,24]. The highest reported P_r in the HZO is 26 μC cm^{-2} (with switching polarization of 45 μC cm^{-2}), using a TiN capping layer of at least 90 nm[21]. In our 5-nm-thick HZO films, P_r also reaches record values of around 34 μC cm^{-2} (P_r = 50 μC cm^{-2} before subtracting the non-ferroelectric switching contribution, as seen in Supplementary Fig. 7)[20] compared to other epitaxial PLD. These values are large even when compared with very good conventional perovskites, such as unstrained $BaTiO_3$ (ref. [45]). However, for the thicker 9 nm film, P_r drops to 18 μC cm^{-2}. This finding can be rationalized by our TEM observations showing that the minority (001)-oriented domains (Fig. 3b) and m-phase (non-ferroelectric), which are absent or very rarely found in the thinnest sample, gradually appear with increasing thickness (Supplementary Fig. 4). It is interesting to note that the ferroelectric loops are obtained readily after growth (see Supplementary Fig. 6), without the technologically inconvenient wake-up cycling required for other HZO systems[46,47], indicating that the ferroelectric rhombohedral phase is stabilized by compressive epitaxial strain.

Density functional theory calculations

Finally, we resorted to first-principles simulations to try to identify the rhombohedral HZO phase observed in our films. Since we are not aware of any previous report on a polar rhombohedral polymorph of HZO, we ran a blind search for (meta)stable structures, using the genetic-algorithm approach implemented in USPEX[48–50]. For this we employed standard first-principles methods, based on density functional theory, and a simulation supercell of 12 atoms (see Methods for details). We ran our search for pure HfO_2 and pure ZrO_2 compositions in bulk-like conditions. We obtained in both cases an $R3m$ structure with a small polarization of the order of 0.1 μC cm^{-2}. Furthermore, for the HfO_2 composition we also found a second polymorph with $R3$ symmetry and a polarization of 41 μC cm^{-2}. These rhombohedral phases lie above the $P2_1/c$ bulk ground state that is usually discussed in the literature on HfO_2, which explains why they have not been previously reported or observed. More precisely, from our calculations we obtain $E(R3m) - E(P2_1/c) = 158$ meV f.u.$^{-1}$ and $E(R3) - E(P2_1/c) = 195$ meV f.u.$^{-1}$ for HfO_2. Note that the polar $Pca2_1$ phase of hafnia discussed in the literature is also more stable than these rhombohedral polymorphs, as we obtain $E(Pca2_1) - E(P2_1/c) = 64$ meV f.u.$^{-1}$ (in agreement with ref. [31], which reports 62 meV f.u.$^{-1}$ for this energy gap). More details on these structures are provided as Supplementary Information.

We then considered these two rhombohedral structures with the HZO composition, discovering that on substitution of Hf by Zr, the $R3$ phase loses its stability in favour of the weakly polar $R3m$ polymorph. We studied several Hf–Zr arrangements compatible with the three-fold symmetry, and observed that the $R3$ destabilization occurs in all cases. The $R3m$ phase of bulk-like HZO is characterized by $d_{111} \approx 2.94$ Å and $P \approx 1$ μC cm^{-2}. Then, we examined the effect of epitaxial compression by running simulations for a number of fixed values of the lattice constants in the (111) plane of the HZO $R3m$ structure, allowing for the relaxation of atoms and the out-of-plane lattice vector. As shown in Fig. 5a, for an epitaxial compression corresponding to an out-of-plane $d_{111} \approx 3.25$ Å, we observe a clear structural transition to a phase that retains the $R3m$ symmetry but is strongly polar, with $P \approx 15$ μC cm^{-2}. This d_{111} value is within the range of what we observe in our thinnest HZO films (for our films with thickness between 1.5 nm and 9 nm, we estimate d_{111} values ranging between ~3.27 Å and 2.98 Å, respectively, from the XRD measurements in Fig. 1b). A definitive comparison between theory and experiment is not yet possible because of possible phase coexistence in our films as they become thicker. Nevertheless, although our computational models do not include effects (crystallite size; surfaces and interfaces; local deviations from the average composition) that could help to stabilize particular phases, our results do suggest that our predicted $R3m$ phase under epitaxial compression (Fig. 5b–d), and even the $R3$ polymorph predicted in the Hf-rich limit, may be approximate representations of the rhombohedral structure in our actual samples (Supplementary Fig. 8).

Strain and nanoparticle pressure stabilize ferroelectricity

In general, we can expect epitaxial strain to lower the symmetry of the films. Thus, obtaining a rhombohedral unit cell under isotropic epitaxial strain would imply an initially cubic or rhombohedral crystallite. The present results therefore allow us to propose a model for the formation of the as-grown ferroelectric phase reported here, as follows. PLD growth of the thin films at high temperature enables the in situ crystallization of HZO. As previously proposed for hafnia-based ferroelectrics, the small particle sizes induce the formation of low-volume fluorite-like phases (either tetragonal or cubic)[39–41]. A plane-view bright-field TEM image (Supplementary Fig. 9) from a 9 nm HZO film shows an average grain size of ~10 nm. Our experiments strongly suggest that in the initial stages of the growth, after the formation of a fully coherent, atomically thin interfacial layer, the internal pressure due to the small particle size favours the undistorted cubic phase. As established by Demkov and Navrotsky[51], the

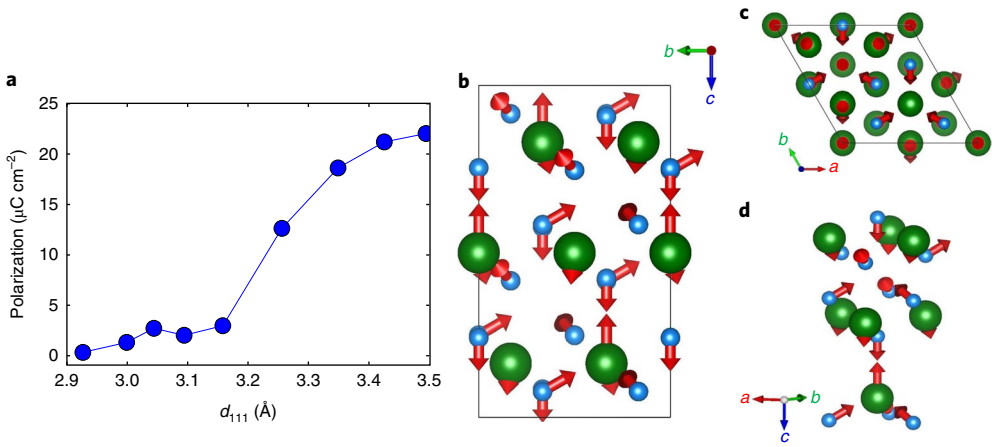

Fig. 5 | Theoretical calculations and proposed structure. a, Computed polarization of the *R*3*m* phase of HZO as a function of d_{111}. Note that we simulate epitaxial strain, and thus control d_{111}, as described in the text, where larger d_{111} values correspond to smaller in-plane lattice constants. **b**,**c**, Two views of the *R*3*m* phase obtained for epitaxially compressed HZO and HfO_2. Green (cyan) spheres represent Hf/Zr (O) atoms. The arrows show the polar distortion with respect to a reference paraelectric structure with $R\bar{3}m$ symmetry, which we deduce by appropriately symmetrizing the *R*3*m* state. **d**, Detailed view of the Hf/Zr–O groups that characterize the *R*3*m* structure, allowing the main polar displacements, and how they preserve the three-fold axis, to be more easily appreciated.

(111) crystal face of ZrO_2 and HfO_2 is energetically favourable, so cubic crystallites growing with that orientation are expected. Due to the favourable epitaxial relationships induced by the STO/LSMO stack (see Fig. 3a), the growing crystallites are subjected to a large epitaxial compressive strain that elongates the cubic unit cell along the out-of-plane [111] direction, inducing rhombohedral symmetry with a polar unit cell (as shown by the synchrotron XRD and ferroelectric characterization).

Increasing the thickness allows the crystal size to grow, relieving the internal pressure, thus favouring the monoclinic bulk structure. At the same time, the presence of the secondary m-phase also helps to release the elastic energy of the compressively strained structure. Even though XRD shows only traces of the m-phase for thicknesses above ~10 nm, the TEM analysis shows that monoclinic (001)-oriented crystallites are already present in the 9-nm-thick film (Supplementary Fig. 4).

While the stabilization of a high-lying rhombohedral polymorph of HZO may seem surprising, similar achievements have been accomplished for other ferroelectric thin films (for example, the super-tetragonal phase of perovskite oxide $BiFeO_3$ on compressive substrates[52]). Moreover, the polymorphic character of HfO_2 and ZrO_2 should facilitate the stabilization of unconventional structures under epitaxial constraints. The evolution of the polarization with the epitaxial constraint reported here (Fig. 5 and Supplementary Fig. 10) mimics the behaviour that is typical among ferroelectric perovskite oxides[53,54], suggesting that the connections between these two families should be further explored.

Outlook

We show that strain engineering can be used in very thin films of HZO to induce a ferroelectric rhombohedral phase, with a large P_r of 34 μC cm^{-2}. Further work is required to tackle issues associated with the strain requisite, such as larger coercive fields or more complex integration in three-dimensional architectures. The insights gained in this work provide the missing clues in the understanding of robust ferroelectricity in thin hafnia-based systems, and also help to overcome one of the main issues for their device utilization: the wake-up cycling. Our theoretical calculations predict an even larger polarization for the rhombohedral phases of Hf-rich compositions, and comparable values for epitaxially compressed HZO structures. In addition, this work suggests a pathway to generate large ferroelectric polarization in nanocrystallites of simple oxides, whose rich phase diagrams include cubic, tetragonal and rhombohedral phases, and in particular in materials with a clear preference for one specific crystal orientation. These highly oriented cubic phases can be stabilized during growth and deformed into a polar structure via epitaxial strain. Furthermore, the highly epitaxial growth of ultrathin ferroelectric hafnia-based films on LSMO has great potential for multiferroic tunnel junctions.

Online content

Any methods, additional references, Nature Research reporting summaries, source data, statements of data availability and associated accession codes are available at https://doi.org/10.1038/s41563-018-0196-0.

Received: 29 January 2018; Accepted: 14 September 2018;
Published online: 22 October 2018

References

1. Scott, J. F. Applications of modern ferroelectrics. *Science* **315**, 954–959 (2007).
2. Ramesh, R. Ferroelectrics: a new spin on spintronics. *Nat. Mater.* **9**, 380–381 (2010).
3. Eom, C. B. & Trolier-McKinstry, S. Thin-film piezoelectric MEMS. *MRS Bull.* **37**, 1007–1017 (2012).
4. Batra, I. P., Wurfel, P. & Silverman, B. D. Phase transition, stability, and depolarization field in ferroelectric thin films. *Phys. Rev. B* **8**, 3257–3265 (1973).
5. Wurfel, P. & Batra, I. P. Depolarization-field-induced instability in thin ferroelectric film-experiment and theory. *Phys. Rev. B* **8**, 5126 (1973).
6. Park, M. H. et al. Ferroelectricity and antiferroelectricity of doped thin HfO_2-based films. *Adv. Mater.* **27**, 1811–1831 (2015).
7. Ohtaka, O. et al. Phase relations and volume changes of hafnia under high pressure and high temperature. *J. Am. Ceram. Soc.* **84**, 1369–1373 (2001).
8. Ohtaka, O. et al. Phase relations and equations of state of ZrO_2 under high temperature and high pressure. *Phys. Rev. B* **63**, 174108 (2001).
9. Lee, C.-K., Cho, E., Lee, H.-S., Hwang, C. S. & Han, S. First-principles study on doping and phase stability of HfO_2. *Phys. Rev. B* **78**, 012102 (2008).
10. Shandalov, M. & McIntyre, P. C. Size-dependent polymorphism in HfO_2 nanotubes and nanoscale thin films. *J. Appl. Phys.* **106**, 084322 (2009).
11. Tsunekawa, S., Ito, S., Kawazoe, Y. & Wang, J. T. Critical size of the phase transition from cubic to tetragonal in pure zirconia nanoparticles. *Nano Lett.* **3**, 871–875 (2003).
12. Hasegawa, H. Rhombohedral phase produced in abraded surfaces of partially stabilized zirconia (PSZ). *J. Mater. Sci. Lett.* **2**, 91–93 (1983).
13. Hasegawa, H. & Hioki, T. Cubic-to-rhombohedral phase transformation in zirconia by ion implantation. *J. Mater. Sci. Lett.* **4**, 1092 (1985).

14. Zhao, B., Jak, E. & Hayes, P. C. Phase equilibria in the system. *J. Less Common Met.* **17**, 151–159 (1969).
15. Burke, D. P. & Rainforth, W. M. Intermediate rhombohedral (r-ZrO2) phase formation at the surface of sintered Y-TZP's. *J. Mater. Sci. Lett.* **16**, 883–885 (1997).
16. Kisi, E. H., Howard, C. J. & Hill, R. J. Crystal structure of orthorhombic zirconia in partially stabilized zirconia. *J. Am. Ceram. Soc.* **72**, 1757–1760 (1989).
17. Müller, J. et al. Ferroelectric hafnium oxide: A CMOScompatible and highly scalable approach to future ferroelectric memories. In *Proc. IEEE Int. Electron Devices Meeting* 10.8.1–10.8.4 (IEEE, 2013).
18. Starschich, S., Griesche, D., Schneller, T. & Böttger, U. Chemical solution deposition of ferroelectric hafnium oxide for future lead free ferroelectric devices. *ECS J. Solid State Sci. Technol.* **4**, P419–P423 (2015).
19. Xu, L. et al. Kinetic pathway of the ferroelectric phase formation in doped HfO_2 films. *J. Appl. Phys.* **122**, 124104 (2017).
20. Shimizu, T., Kata, K., Kiguchi, T., Akama, A. & Konno, T. J. The demonstration of significant ferroelectricity in epitaxial Y-doped HfO_2 film. *Sci. Rep.* **6**, 32931 (2016).
21. Kim, S. J. et al. Large ferroelectric polarization of $TiN/Hf_{0.5}Zr_{0.5}O_2/TiN$ capacitors due to stress-induced crystallization at low thermal budget. *Appl. Phys. Lett.* **111**, 242901 (2017).
22. Hyuk Park, M. et al. Effect of forming gas annealing on the ferroelectric properties of $Hf_{0.5}Zr_{0.5}O_2$ thin films with and without Pt electrodes. *Appl. Phys. Lett.* **102**, 112914 (2013).
23. Park, M. H. et al. Study on the degradation mechanism of the ferroelectric properties of thin $Hf_{0.5}Zr_{0.5}O_2$ films on TiN and Ir electrodes. *Appl. Phys. Lett.* **105**, 72902 (2014).
24. Hoffmann, M. et al. Stabilizing the ferroelectric phase in doped hafnium oxide. *J. Appl. Phys.* **118**, 072006 (2015).
25. Florent, K. et al. Understanding ferroelectric Al:HfO_2 thin films with Si-based electrodes for 3D applications. *J. Appl. Phys.* **121**, 204103 (2017).
26. Böscke, T. S., Müller, J., Bräuhaus, D., Schröder, U. & Böttger, U. Ferroelectricity in hafnium oxide thin films. *Appl. Phys. Lett.* **99**, 102903 (2011).
27. Starschich, S., Schenk, T., Schroeder, U. & Boettger, U. Ferroelectric and piezoelectric properties of $Hf_{1-x}Zr_xO_2$ and pure ZrO_2 films. *Appl. Phys. Lett.* **110**, 182905 (2017).
28. Shimizu, T. et al. Study on the effect of heat treatment conditions on metalorganic-chemical-vapor-deposited ferroelectric $Hf_{0.5}Zr_{0.5}O_2$ thin film on Ir electrode. *Jpn. J. Appl. Phys.* **53**, 09PA04 (2014).
29. Park, M. H., Kim, H. J., Kim, Y. J., Moon, T. & Hwang, C. S. The effects of crystallographic orientation and strain of thin $Hf_{0.5}Zr_{0.5}O_2$ film on its ferroelectricity. *Appl. Phys. Lett.* **104**, 072901 (2014).
30. Shiraishi, T. et al. Impact of mechanical stress on ferroelectricity in $(Hf_{0.5}Zr_{0.5})O_2$ thin films. *Appl. Phys. Lett.* **108**, 262904 (2016).
31. Materlik, R., Künneth, C. & Kersch, A. The origin of ferroelectricity in $Hf_{1-x}Zr_xO_2$: A computational investigation and a surface energy model. *J. Appl. Phys.* **117**, 134109 (2015).
32. Park, M. H. et al. Surface and grain boundary energy as the key enabler of ferroelectricity in nanoscale hafnia-zirconia: a comparison of model and experiment. *Nanoscale* **9**, 9973–9986 (2017).
33. Müller, J. et al. Ferroelectricity in simple binary ZrO_2 and HfO_2. *Nano Lett.* **12**, 4318–4323 (2012).
34. Müller, J. et al. Ferroelectric $Zr_{0.5}Hf_{0.5}O_2$ thin films for nonvolatile memory applications. *Appl. Phys. Lett.* **99**, 112901 (2011).
35. Park, M. H., Kim, H. J., Kim, Y. J., Lee, W. & Moon, T. Evolution of phases and ferroelectric properties of thin $Hf_{0.5}Zr_{0.5}O_2$ films according to the thickness and annealing temperature. *Appl. Phys. Lett.* **102**, 242905 (2013).
36. Riedel, S., Polakowski, P. & Müller, J. A thermally robust and thickness independent ferroelectric phase in laminated hafnium zirconium oxide. *AIP Adv.* **6**, 095213 (2016).
37. Morozovska, A. N., Glinchuk, M. D. & Eliseev, E. A. Phase transitions induced by confinement of ferroic nanoparticles. *Phys. Rev. B* **76**, 014102 (2007).
38. Polking, M. J. et al. Size-dependent polar ordering in colloidal GeTe nanocrystals. *Nano Lett.* **11**, 1147–1152 (2011).
39. Lu, C. H., Raitano, J. M., Khalid, S., Zhang, L. & Chan, S. W. Cubic phase stabilization in nanoparticles of hafnia-zirconia oxides: Particle-size and annealing environment effects. *J. Appl. Phys.* **103**, 124303 (2008).
40. Shen, P. & Lee, W. H. (111)-Specific coalescence twinning and martensitic transformation of tetragonal ZrO_2 condensates. *Nano Lett.* **1**, 707–711 (2001).
41. Vollath, D., Fischer, F. D., Hagelstein, M. & Szabó, D. V. Phases and phase transformations in nanocrystalline ZrO2. *J. Nanopart. Res.* **8**, 1003–1016 (2006).
42. Huan, T. D., Sharma, V., Rossetti, G. A. & Ramprasad, R. Pathways towards ferroelectricity in hafnia. *Phys. Rev. B* **90**, 064111 (2014).
43. Pešić, M. et al. Physical mechanisms behind the field-cycling behavior of HfO_2-based ferroelectric capacitors. *Adv. Funct. Mater.* **26**, 4601–4612 (2016).
44. Garcia-Barriocanal, J. et al. Colossal Ionic conductivity at interfaces of epitaxial ZrO_2:Y_2O_3/$SrTiO_3$ heterostructures. *Science* **321**, 676–680 (2008).
45. Lee, H. N., Christen, H. M., Chisholm, M. F., Rouleau, C. M. & Lowndes, D. H. Strong polarization enhancement in asymmetric three-component ferroelectric superlattices. *Nature* **433**, 395–399 (2005).
46. Kim, H. J. et al. A study on the wake-up effect of ferroelectric $Hf_{0.5}Zr_{0.5}O_2$ films by pulse-switching measurement. *Nanoscale* **8**, 1383–1389 (2015).
47. Schenk, T. et al. Electric field cycling behavior of ferroelectric hafnium oxide. *ACS Appl. Mater. Interfaces* **6**, 19744–19751 (2014).
48. Lyakhov, A. O., Oganov, A. R., Stokes, H. T. & Zhu, Q. New developments in evolutionary structure prediction algorithm USPEX. *Comput. Phys. Commun.* **184**, 1172–1182 (2013).
49. Oganov, A. R. & Glass, C. W. Crystal structure prediction using ab initio evolutionary techniques: Principles and applications. *J. Chem. Phys.* **124**, 244704 (2006).
50. Glass, C. W., Oganov, A. R. & Hansen, N. USPEX—Evolutionary crystal structure prediction. *Comput. Phys. Commun.* **175**, 713–720 (2006).
51. Demkov, A. & Navrotsky, A. *Materials Fundamentals of Gate Dielectrics* (Springer, Dordrecht, 2005).
52. Béa, H. et al. Evidence for room-temperature multiferroicity in a compound with a giant axial ratio. *Phys. Rev. Lett.* **102**, 217603 (2009).
53. Tinte, S., Rabe, K. M. & Vanderbilt, D. Anomalous enhancement of tetragonality in $PbTiO_3$ induced by negative pressure. *Phys. Rev. B* **68**, 144105 (2003).
54. Wojdeł, J. C. & Íñiguez, J. Ab initio indications for giant magnetoelectric effects driven by structural softness. *Phys. Rev. Lett.* **105**, 037208 (2010).

Acknowledgements

We are grateful to S. Volkov and F. Bertram for their help at the P08 beamline in Petra III (DESY0-Hamburg), and T. Schenk for insightful discussions about the paper. Y.W. and B.N. are grateful for China Scholarship Council and Van Gogh travel grants. P.N. acknowledges the funding received from the European Union's Horizon 2020 research and innovation programme under Marie Sklodowska-Curie grant agreement no. 794954. P.N. and B.D. would like to acknowledge a public grant overseen by the French National Research Agency (ANR) as a part of the `Investissements d'Avenir' programme (grant no. ANR-10-LABX-0035, Labex Nanoscalay) and through project ANR-17-CE24-0032/EXPAND. B.D. also acknowledges Luxembourg National Research Fund under Project MULTICALOR:INTER/MOBILITY/16/11259210. H.J.Z. and J.Í. acknowledge the support of the Luxembourg National Research Fund through the PEARL (grant no. FNR/P12/4853155/Kreisel COFERMAT) and CORE (grant no. FNR/C15/MS/10458889 NEWALLS) programmes.

Author contributions

B.N. and Y.W. conceived the idea, and the project plan. Y.W. synthesized the films. P.N. and J.M. prepared samples for TEM, and performed the experiments, and P.N. analysed the data, under the supervision of B.J.K. and B.D. Y.W., M.S. and B.N. performed XRD and analysed the data. Y.W., S.M. and G.A. fabricated devices, tested their ferroelectric properties and analysed the data with help from A.S.E. H.J.Z. and J.Í. performed the first-principles calculations. B.J.K. and G.R.B. extensively helped in understanding the structure and symmetry of the films. P.L. and B.D. provided useful insights all along the project. Y.W., P.N., B.N. and J.Í. co-wrote the manuscript with feedback from all of the authors.

Competing interests

The authors declare no competing interests.

Additional information

Supplementary information is available for this paper at https://doi.org/10.1038/s41563-018-0196-0.

Reprints and permissions information is available at www.nature.com/reprints.

Correspondence and requests for materials should be addressed to B.N.

Publisher's note: Springer Nature remains neutral with regard to jurisdictional claims in published maps and institutional affiliations.

Methods

Thin-film synthesis. Thin films of HZO with thicknesses in the range of 1.5–27 nm were grown by PLD on LSMO-buffered (001)-STO substrates. A KrF excimer laser with a wavelength of 248 nm was used to ablate polycrystalline targets of LSMO (purchased from PI-KEM, as the bottom electrode) and sequentially, HZO (home-made). LSMO was deposited using a laser fluence of 1 J cm^{-2} and a laser frequency of 1 Hz under a 0.15 mbar oxygen atmosphere and a substrate temperature of 775 °C. A ceramic HZO target (monoclinic $P2_1/c$ phase) was synthesized at 1,400 °C by solid-state reaction, starting from HfO_2 (99% purity) and ZrO_2 (99.5% purity) powders. A fluence of 1.1 J cm^{-2} and repetition rate of 2 Hz was employed to grow the HZO films. The deposition was performed in an oxygen pressure of 0.1 mbar while keeping the substrates at a temperature of 800 °C. After deposition, the film was cooled down to room temperature at a rate of 5 °C min^{-1} under an oxygen pressure of 300 mbar.

X-ray structural characterization. The structure and orientation of the films was characterized by XRD, using a Panalytical X'pert Pro diffractometer operating in two modes: using the line focus of the incident beam for high-resolution θ–2θ specular scans, which provide the lattice parameters; and using the point focus of the incident beam, for high-intensity/medium-resolution measurements of pole figures, which involve scanning φ (azimuthal angle) and χ (tilt of the sample plane around the incident beam direction) while the detector is fixed at a particular Bragg reflection. Synchrotron diffraction measurements were performed at the P08 High Resolution Diffraction Beamline in PETRA III, with a wavelength of $\lambda = 1.378$ Å, using a Kohzu six-circle diffractometer and a two-dimensional Pilatus 100k detector.

Electron microscopy and EDS. Cross-sectional and plan-view specimens for electron microscopy were prepared via the standard procedure of mechanical grinding and polishing the samples down to 100 µm, and dimpling (Gatan) followed by ion milling (PIPS II) to electron transparency. Some cross-sections were also prepared via the focused ion beam (Helios 660 ThermoFischer Scientific) technique, and both preparations yielded similar results. Electron microscopy and EDS were performed on a Titan G2, Cs-corrected TEM equipped with an extreme field-emission gun and a Super X EDS system with four solid-state detectors placed symmetrically along the optical axes. Atomic-resolution imaging was performed in the HAADF-STEM mode, where the intensity in the image is ~Z^2, thus yielding a clear atomic number contrast. Images were analysed using ImageJ, TIA-ES Vision and Digital micrograph. EDS was performed simultaneously with image acquisition in the HAADF-STEM mode. Chemical maps were acquired for 30 min with conditions optimized and collected at thousands of X-ray photons per second, and analysed using Bruker e-spirit software.

Electrical measurements. LSMO top electrodes were deposited by PLD with the same growth condition as the bottom LSMO electrodes, as described in the `Thin-film synthesis' section. LSMO top-electrode pads with different sizes were processed by physical etching (ion milling). Planar LSMO/HZO/LSMO capacitors were measured using a ferroelectric tester (AiXACCT, TF analyser 2000). The ferroelectric response of the films was tested via PUND[55] measurements, which are able to separate switching currents from other contributions.

Simulation methods. For our structural predictions, we used the USPEX code[48–50], which is based on genetic algorithms. We applied this method to search for possible rhombohedral phases of HfO_2 and ZrO_2 in bulk-like conditions. We considered 12-atom cells for HfO_2 and ZrO_2. After the blind structural search, we ran additional first-principles simulations for HfO_2, ZrO_2 and HZO compositions focusing on the discovered $R3$ and $R3m$ phases. For the HZO composition, we considered several representative Hf/Zr arrangements that preserve the three-fold rotation axis, using a 72-atom cell.

Our first-principles simulations were carried out using the VASP (Vienna Ab initio Simulation Package) code[56,57]. We used the PBEsol approximation to density functional theory[58]. Atomic cores were treated within the projector-augmented wave approach[59], and we solved explicitly for the following electrons: 5p, 6s and 5d for Hf; 4s, 4p, 5s and 5d electrons for Zr; and 2s and 2p electrons for O. We represented the electronic wavefunctions in a plane-wave basis, cutoff at 500 eV. For the ground state of the bulk HfO_2 ($P2_1/c$) with lattice parameters (a, b, c) of about (5.1, 5.2, 5.2) Å, a mesh of 8×8×8 k-points was used for Brillouin zone integrations; similarly dense grids were used in all other simulations in this work. When doing the structural relaxation, the calculations were stopped for residual forces below 0.005 eV A^{-1}. To simulate the effect of epitaxial strain, we used a hexagonal-like cell with in-plane lattice vectors forming an angle of 120°, and the third lattice vector perpendicular to the plane. The in-plane vectors were fixed at a series of values, smaller ones corresponding to stronger in-plane compression; then the out-of-plane vector, and the atomic positions, were relaxed.

We tested the influence of the density functional in our results by solving selected structures (for the predicted polar rhombohedral phase) using the local-density approximation (LDA). As shown in Supplementary Fig. 10, the comparison between PBEsol and LDA results reflects the well-known LDA over-binding problem (that is, slight underestimation of lattice constants and cell volumes); otherwise, our results and conclusions are the same irrespective of the functional employed.

We made extensive use of crystallographic servers[60–62] and the VESTA[63] visualization program. We computed polarizations by comparing the polar structures with properly symmetrized, paraelectric states that we use as a reference. Initially we used the Berry phase formalism to compute the polarization from first principles[64], and acquired essentially identical results to those obtained by computing the total dipole based on nominal ionic charges; hence, we used the latter method for most of our later calculations.

Data availability

The data that support the findings of this study are included in the main text and Supplementary Information.

References

55. Rabe, K. M, Ahn, C. H. & Triscone, J.-M. (eds) *Physics of Ferroelectrics: A Modern Perspective* (Springer,Berlin, 2007) .
56. Kresse, G. & Furthmüller, J. Efficient iterative schemes for ab initio total-energy calculations using a plane-wave basis set. *Phys. Rev. B* **54**, 11169–11186 (1996).
57. Joubert, D. From ultrasoft pseudopotentials to the projector augmented-wave method. *Phys. Rev. B* **59**, 1758–1775 (1999).
58. Perdew, J. et al. Atoms, molecules, solids, and surfaces: applications of the generalized gradient approximation for exchange and correlation. *Phys. Rev. B* **46**, 6671–6687 (1992).
59. Blöchl, P. E. Projector augmented-wave method. *Phys. Rev. B* **50**, 17953–17979 (1994).
60. Stokes, H. T. & Hatch, D. M. FINDSYM: Program for identifying the space-group symmetry of a crystal. *J. Appl. Crystallogr.* **38**, 237–238 (2005).
61. Capillas, C. et al. A new computer tool at the Bilbao Crystallographic Server to detect and characterize pseudosymmetry. *Zeitschrift Krist.* **226**, 186–196 (2011).
62. Orobengoa, D., Capillas, C., Aroyo, I. & Perez, J. M. AMPLIMODES: symmetry mode analysis on the Bilbao Crystallographic Server research papers. *Appl.Cryst.* **42**, 820–833 (2009).
63. Momma, K. & Izumi, F. VESTA 3 for three-dimensional visualization of crystal, volumetric and morphology data. *J. Appl. Crystallogr.* **44**, 1272–1276 (2011).
64. King-Smith, R. D. & Vanderbilt, D. Theory of polarization of crystalline solids. *Phys. Rev. B* **47**, 1651–1654 (1993).